Available online at www.sciencedirect.com
ScienceDirect
Surface Science 600 (2006) 4613–4621
SURFACE SCIENCE
www.elsevier.com/locate/susc

Characterization of a bioactive nanotextured surface created by controlled chemical oxidation of titanium

Ji-Hyun Yi [a], Caroline Bernard [a], Fabio Variola [a,b], Sylvia F. Zalzal [a], James D. Wuest [c], Federico Rosei [b], Antonio Nanci [a,*]

[a] *Laboratory for the Study of Calcified Tissues and Biomaterials, Faculté de Médecine Dentaire, Université de Montréal, Montréal, QC, Canada H3C 3J7*
[b] *INRS-EMT, Université du Québec, 1650 Boul. Lionel-Boulet, Varennes, QC, Canada J3X 1S2*
[c] *Département de Chimie, Université de Montréal, Montréal, QC, Canada H3C 3J7*

Received 15 March 2006; accepted for publication 25 July 2006
Available online 22 August 2006

Abstract

Events at bone–implant interfaces are influenced by implant surface properties. Our previous work has revealed that osteogenic activity is enhanced by a nanotextured Ti surface, obtained by controlled chemical oxidation using a H_2SO_4/H_2O_2 mixture. To better understand the origin of this biological effect, we have carried out a characterization of the modified surface at the nanoscale. In particular, the morphology, structure, and chemical composition of the Ti surface were examined thoroughly. X-ray photoelectron spectroscopy (XPS), combined with grazing-angle Fourier-transform infrared (FTIR) spectroscopy, revealed that the oxidized Ti surface consists of almost pure TiO_2 with Ti:O ratio ranging between 1:2.02 and 1:2.08. Raman spectroscopy and X-ray diffraction (XRD) indicated that the chemically treated Ti surface is mainly composed of amorphous titania. Scanning electron microscopy (SEM) clearly showed that the treated Ti substrate becomes highly porous and has a surface consisting of nano-sized pits, which have average diameters and fractal dimensions ranging between 20–22 nm and 1.11–1.17, respectively. Atomic force microscopy (AFM) revealed a three–fold increase in surface roughness. The thickness of the oxide layer on the treated Ti surface is estimated to be ~32–40 nm. Together, these observations provide a detailed characterization of chemically oxidized Ti surfaces at the nanoscale and offer new prospects for understanding and controlling the relationship between the properties of materials and their interactions with cells. Our work brings us closer to the creation of "intelligent" implant surfaces, capable of selectively influencing cell behavior.

Keywords: Nanotopography; Titanium oxides; Chemical oxidation; SEM; AFM; FTIR; XPS

1. Introduction

Millions of orthopedic and dental implants are used each year to replace or restore function to diseased and damaged tissues. Because the surface of an implant plays an extremely important role in determining biocompatibility and facilitating tissue integration [1,2], there have been many attempts to modify it [3–10]. The bone matrix into which implants are placed possesses an intrinsic nanotopography [11,12]. In particular, hydroxyapatite and collagen, which are the major building blocks of bone, offer osteoblasts an extracellular matrix surface with a high degree of nanoscale roughness [13]. However, currently used implant materials composed of micro-size grains, whether metallic or ceramic, exhibit surfaces that are fairly smooth at the nanoscale (RMS roughness < 5 nm).

Various cell types have been shown to respond to nanotopography, and increased responses have been reported for cells grown on nanophase metal oxides [14,15], polymers with nanotopography [16,17], nanometric carbon fibers [18], and nanosize patterns [19–21]. In addition, results

* Corresponding author. Tel.: +1 514 343 5846; fax: +1 514 343 2233.
E-mail address: antonio.nanci@umontreal.ca (A. Nanci).

0039-6028/$ - see front matter © 2006 Elsevier B.V. All rights reserved.
doi:10.1016/j.susc.2006.07.053

from a recent animal study show that nanotextured Ti improves bone–implant contact [22]. These observations suggest that if surface features are to be perfected, they must optimize, at the nanoscale, the various cell/matrix/substrate interactions that regulate cell attachment, migration, differentiation, and gene expression [23].

We have shown that controlled chemical oxidation of Ti using a mixture of H_2SO_4/H_2O_2 yields a nanotextured surface [5]. The resulting nanotopography significantly influences the very early stages of *in vitro* osteogenesis [24]. Such an early effect is needed to control the healing cascade from the very start. It is expected that the bioactivity of our textured Ti surface can be further enhanced by controlling its surface properties at the nanoscale. The effort to establish a clear relationship between a specific characteristic of the nanostructured Ti surface and tissue regeneration must begin with a detailed analysis of the surface. The present work reports a physicochemical characterization of a nanotextured TiO_2 surface obtained by controlled chemical oxidation. Detailed features of surface morphology were analyzed at the nanometer scale. The crystalline phase and chemical composition were determined, and the thickness and structure of the TiO_2 layer were examined.

2. Materials and methods

2.1. Controlled chemical oxidation of Ti discs

The test samples consisted of commercially pure grade 2 Ti discs (cpTi) with a diameter of 14 mm and a height of 2 mm, polished to a mirror finish. The discs were supplied by DePuy (Warsaw, IN). The cpTi samples were cleaned with toluene (Fisher Scientific, Fair Lawn, NJ) in an ultrasonic bath and dried in air. They were then treated with a 50:50 mixture of 37 N sulfuric acid (J.T. Baker, Phillipsburg, NJ) and 30% aqueous hydrogen peroxide (Fisher). The components were combined on ice to control the exotherm of mixing, and then the cooling bath was removed to allow the temperature to rise to 22 °C. The discs were then added to the mixture (~10 mL/disc) and kept for 2 h at 22 °C under constant agitation [5]. The oxidized samples were rinsed in distilled water in an ultrasonic bath and air-dried. Four samples were prepared and subsequently characterized under identical conditions. Control discs were simply cleaned successively with toluene and distilled water, then air-dried.

2.2. X-ray photoelectron spectroscopy (XPS)

The chemical composition of control and treated cpTi samples was analyzed by XPS using an ESCALAB 220I-XL spectrophotometer, equipped with an Al Kα (1486.6 eV) monochromatic source at base pressures less than 10^{-8} Torr with a perpendicular take-off angle. High-resolution spectra were charge-compensated by setting the binding energy of the C1s peak to 284.6 eV. Elemental concentrations were estimated by measuring peak areas using CasaXPS (Casa Software Ltd., Cheshire, UK). The thickness d of the native oxide layer on the control cpTi surface was estimated using the following relation [25]:

$$d = \lambda_{\mathrm{TiO}_x} \sin\psi \ln\left(\frac{I_{\mathrm{TiO}_x}}{I_{\mathrm{Ti}}} \cdot \frac{N^{\infty}_{\mathrm{Ti}}\lambda^{\infty}_{\mathrm{Ti}}}{N^{\infty}_{\mathrm{TiO}_x}\lambda^{\infty}_{\mathrm{TiO}_x}} + 1\right) \quad (1)$$

where ψ is the electron take-off angle of the XPS; $\lambda^{\infty}_{\mathrm{TiO}_x}$ and $\lambda^{\infty}_{\mathrm{Ti}}$ are the mean free path of the electrons in the oxide layer and the Ti substrate, respectively; I_{TiO_x} is the Ti_{2p} peak intensity of the oxide layer; I_{Ti} is the Ti_{2p} peak intensity of the underlying Ti substrate attenuated by the oxide layer; and N^{∞}_{Ti} and $N^{\infty}_{\mathrm{TiO}_x}$ are the atomic densities of the Ti atoms in the Ti substrate and oxide layer, respectively.

2.3. Fourier transform infrared spectroscopy (FTIR)

The structure of nanotextured Ti surfaces was investigated by FTIR using a dry air-purged Nexus 870 FTIR spectrometer equipped with a SAGA (Smart Aperture Grazing Angle) accessory (Thermo Nicolet, Madison, WI). Polarized light at an angle of 80° with respect to the surface normal was used to characterize the ultra-thin oxide layer on the cpTi discs. The spectral range was 475–4000 cm^{-1}, the resolution was 4 cm^{-1}, and the number of scans was 256. A gold substrate was used as a reference. Recorded spectra were fitted by PeakFit (SPSS, Chicago, IL) software using Pearson VII functions [26].

2.4. X-ray diffraction (XRD)

The crystallinity of control and treated cpTi surfaces was investigated by XRD using a Philips PANalytical X'Pert Pro diffractometer equipped with a secondary monochromator (Cu Kα radiation, $\lambda = 0.15405$ nm). Grazing-incidence XRD with $\omega/2\theta$ mode was used to investigate the ultra-thin oxide layer on cpTi discs. The incident beam angle (ω) was 0.5° and the range of 2θ was 15°–70°. The step size and set time were 0.02° and 16 s, respectively.

2.5. Raman spectroscopy

Micro-Raman spectroscopy was used to further characterize the bonding states of control and treated cpTi surfaces using a Renishaw Imaging Microscope Wire™. A green line laser (argon-ion excitation $\lambda = 514.5$ nm) was taken as the excitation source. Low laser intensity was used to avoid sample damage. Raman spectra were obtained in the 180° backscattering configuration along the same optical path as the incoming laser at room temperature.

2.6. Morphological analysis

Control and treated Ti surfaces were imaged using a JEOL-JSM7400F field emission scanning electron microscope (SEM) operated at 1–2 kV. Surface topography was observed by atomic force microscopy (AFM) in tap-

ping mode using a JEOL JSPM-5200 at $\sim 10^{-6}$ Torr. Ultrasharp silicon tips (SSS-NCHR, Nanosensors, Neuchatel, Swiss) with a curvature radius of ~2 nm were used to minimize the tip-convolution effect.

SEM and AFM micrographs were analyzed using a commercial image processing program, analySIS® (Soft Imaging System GmbH, Münster, Germany). To determine the size and shape of pits in the micrographs, the thresholds were carefully set to convert digitized 256 gray-scale images into binary images. A perimeter–area relationship of fractal dimension was applied to characterize pits in two dimensions [27]. The perimeter–area relationship for a set of pits is given by:

$$P = kA^{D/2} \tag{2}$$

where P and A are the perimeter and area of a pit, respectively; k is a scaling constant; and D is the fractal dimension. The fractal dimension can be therefore estimated by the slope of the relationship between $\log P$ and $\log A$. Regular objects such as circles and squares have a fractal dimension D equal to 1, whereas highly complex convoluted objects (i.e. high ratio of P/A) have D values approaching 2.

3. Results

3.1. X-ray photoelectron spectroscopy measurements

XPS analyses of cpTi samples before and after chemical oxidation are summarized in Table 1. The chemical composition of the untreated sample surface indicated the presence of naturally formed titanium oxide with some contaminants such as C, N, and Si. After chemical treatment, the composition showed titanium oxide with no contaminants except C, which has previously been observed on oxide layers under atmospheric conditions, often in the form of hydrocarbons [28,29]. It is worth noting that no traces of S were observed, even though the samples were immersed in concentrated H_2SO_4.

High-resolution spectra of the Ti_{2p} core level are presented in Fig. 1. On the untreated cpTi surface (Fig. 1A), a strong doublet with broad shoulders was recorded at about 458.6 eV and 464.3 eV. The doublet is attributed to Ti^{4+}, showing that TiO_2 is the main constituent of the oxide layer [28,30]. Deconvolution of the Ti_{2p} peak confirmed the presence of $Ti^{metallic}$ (peaks at 454.1 and 460.2 eV) and also revealed Ti^{2+} (peaks at 456.6 and 461.3 eV) [28,30,31]. The $Ti^{metallic}$ peaks were attributed to the underlying Ti substrate because the oxide layer is thin. The weak and broad Ti^{2+} peaks indicated that the native oxide layer is a mixture of TiO_2 (~96 wt%) and TiO (~4 wt%). The thickness of this oxide layer, calculated using Eq. (1), was found to be about 5.0 nm, which is a typical value for naturally formed oxide layers on Ti [32].

Table 1
Quantitative surface composition (atomic percentage) of Ti samples as determined by XPS

	Ti	O	C	N	Si
Untreated	11.7	48.5	36.8	1.1	1.9
Oxidized	18.6	51.9	28.7	0.7	0

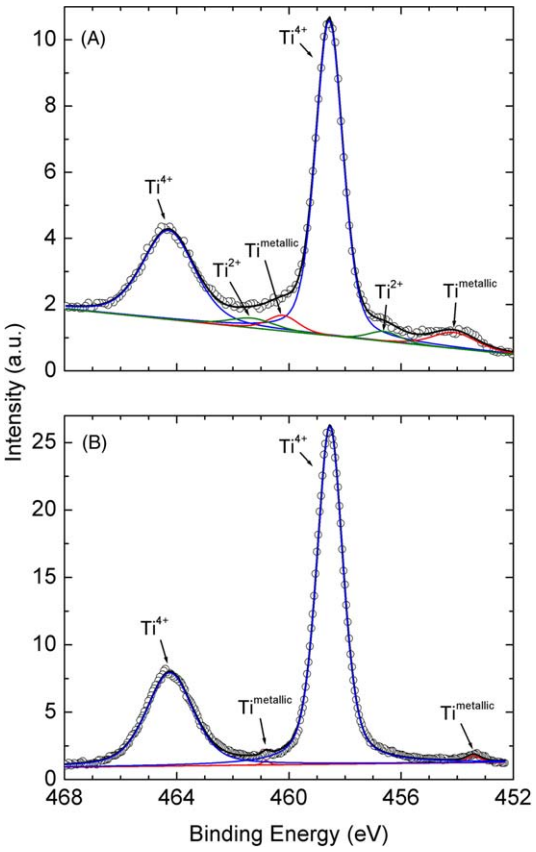

Fig. 1. XPS spectra of the Ti_{2p} core level for untreated (A) and treated (B) Ti surfaces. The various components ($Ti^{metallic}$, Ti^{2+}, and Ti^{4+}) are identified by means of the fit procedure described in Section 2.

Clearly different features of Ti_{2p} were observed after chemical oxidation (Fig. 1B). Only an intense Ti^{4+} doublet was detected and no other forms of titanium oxide were observed, demonstrating that the oxide layer consists of pure TiO_2. Moreover, the ratio of $Ti^{metallic}/Ti^{4+}$ decreases considerably as a result of the treatment, indicating that the thickness of the TiO_2 layer increases significantly.

Fig. 2 displays high-resolution spectra of the O_{1s} core level. Both control and treated Ti samples clearly showed the O_{1s} peak from Ti–O bonds at 530.0 eV [33] with shoulder peaks at higher energy. Deconvolution of the O1s spectra suggested that these shoulders originate from O in OH species (531.6 eV) and adsorbed H_2O (532.5 eV), respectively [30,34]. On the control Ti surface, the fractions of $O1s_{(OH)}$ and $O1s_{(H_2O)}$ were 31.6% and 10.3%, respectively, while they are reduced to 22.7% and 8.1%, respectively, on the modified surface. This difference reveals the lower content of water-related species on the treated surface. XPS analysis with shallow take-off angles may prove to be better for determining whether the water content is really lower on oxidized Ti surfaces or if this is an artifact

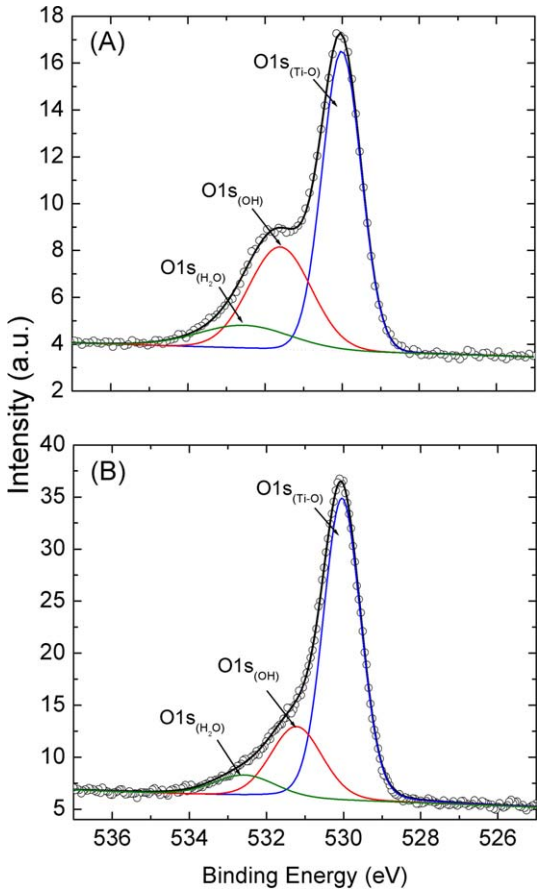

Fig. 2. XPS spectra of the O_{1s} core level for untreated (A) and treated (B) Ti surfaces.

of sampling in a thicker oxide layer. It is worth mentioning that the TiO_2 surface newly generated by chemical treatment still contains a considerable quantity of hydroxyl groups. An increased number of hydroxyl groups are expected to be seen on H_2O_2-treated Ti surfaces [24,35], and this increase has been correlated with an enhancement of apatite nucleation and protein adsorption [35,36].

3.2. Fourier transform infrared spectroscopy

FTIR spectra of cpTi samples before and after chemical treatment are reported in Fig. 3. The spectrum of untreated cpTi is characterized by a broad band around 850 cm^{-1}, which is attributed to Ti–O bonds (Fig. 3A) [37,38]. The broad and weak nature of this Ti–O band reflects the thickness (~5.0 nm) of the layer of naturally formed titanium oxide. Bands at about 1170 cm^{-1} and 1650 cm^{-1} were assigned to carbon-related contaminants such as Ti–O–C and adsorbed water, respectively [26,39]. The FTIR spectrum of treated cpTi (Fig. 3B) showed completely different aspects. Two broad peaks were recorded near 660 cm^{-1} and 830 cm^{-1}, which were assigned to Ti–O bonds [37,38,40]. The integral area of these bands was several times larger than that of untreated cpTi, indicating an important increase in the thickness of the oxide layer after

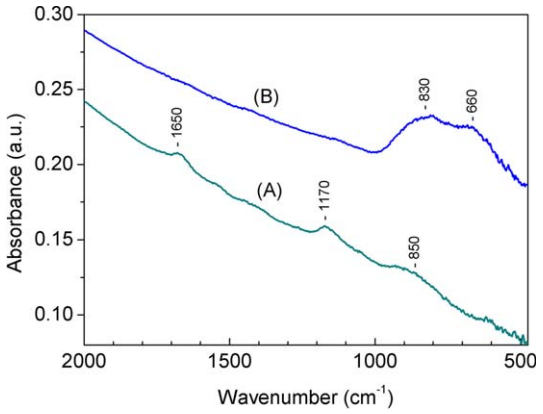

Fig. 3. FTIR spectra of untreated (A) and treated cpTi surfaces (B).

chemical treatment. In addition, the carbon-related impurity band and water band disappeared.

3.3. X-ray diffraction measurements

A typical XRD pattern of the treated cpTi sample is reported in Fig. 4A. In none of our samples were peaks corresponding to titanium oxide observed in XRD patterns. Only the peaks corresponding to α-Ti [XRD Joint

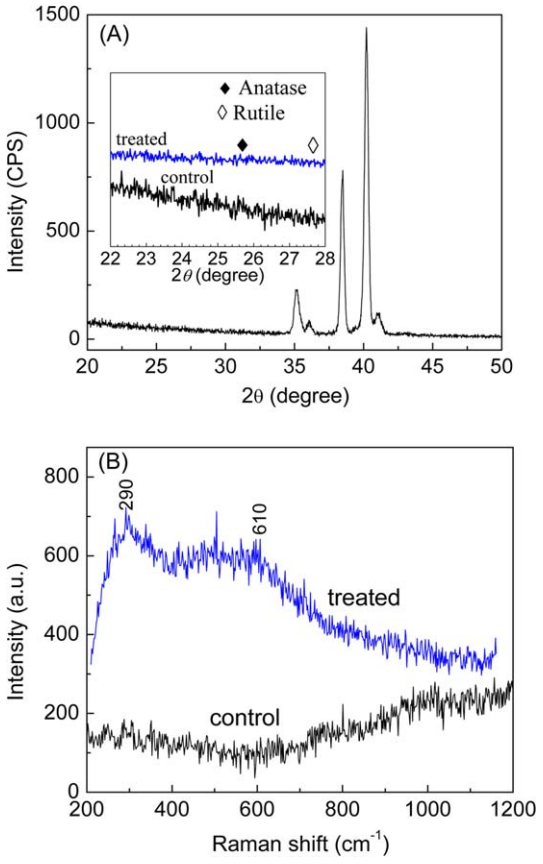

Fig. 4. (A) Grazing angle XRD pattern of a treated cpTi surface. The inset displays XRD patterns of control and treated cpTi in the 2θ range of 22°–28°. (B) Raman spectra of control and treated cpTi.

Committee on Powder Diffraction Standards (JCPDS) data file No. 44-1294] are present. Details of the small angle zone (2θ range of 22°–28°) depicted in the inset in Fig. 4A confirm that neither control nor treated samples exhibit characteristic peaks of the anatase or rutile phases.

3.4. Raman spectroscopy

Raman spectra of cpTi samples before and after chemical treatment are reported in Fig. 4B. The spectrum of the control sample does not show any significant Raman band in the whole frequency range, undoubtedly due to the amorphous nature of the native oxide layer, as well as to its thinness. In contrast, the overall appearance of the Raman spectrum of the treated sample indicates an amorphous layer thicker than that of the control sample, with weak and broad bands at 290 cm^{-1} and 610 cm^{-1}. The attribution of these bands was not clearly determined.

3.5. SEM and AFM

Fig. 5A and B display SEM micrographs of Ti surfaces before and after chemical treatment. When observed at high magnification, the untreated sample was smooth with no topographical features, whereas a distinctive texture characterized by nano-sized pits was clearly seen on the treated cpTi surface. The nanopits were uniformly distributed across the surface of the disc. A more detailed image presented in the inset of Fig. 5B indicates that treated Ti exhibits a three-dimensional sponge–like porosity.

The size and shape of nanopits can be more systematically determined by detailed image analysis by methods described in Section 2. The area, perimeter, and equivalent circle diameter (ECD) of nanopits were measured, and Fig. 5C provides the ECD distribution. The ECD of the nanopits has a Gaussian distribution with an average value of 22 ± 7 nm. Fig. 5D shows the perimeter (P)–area (A) relationship of the nanopits formed on the cpTi surface. A fit demonstrated a clear linear relationship of log P and log A values, with standard deviations of the fit and correlation coefficients of 0.067 and 0.932, respectively. The fractal dimension estimated from the $\log P/\log A$ relationship is 1.17 ± 0.01, which demonstrates that the nanopits have significantly longer perimeters than those of equivalent circles.

Fig. 6 displays the AFM topographies of Ti surfaces before and after chemical etching. At low magnification (3×3 μm^2), only traces of mechanical polishing were

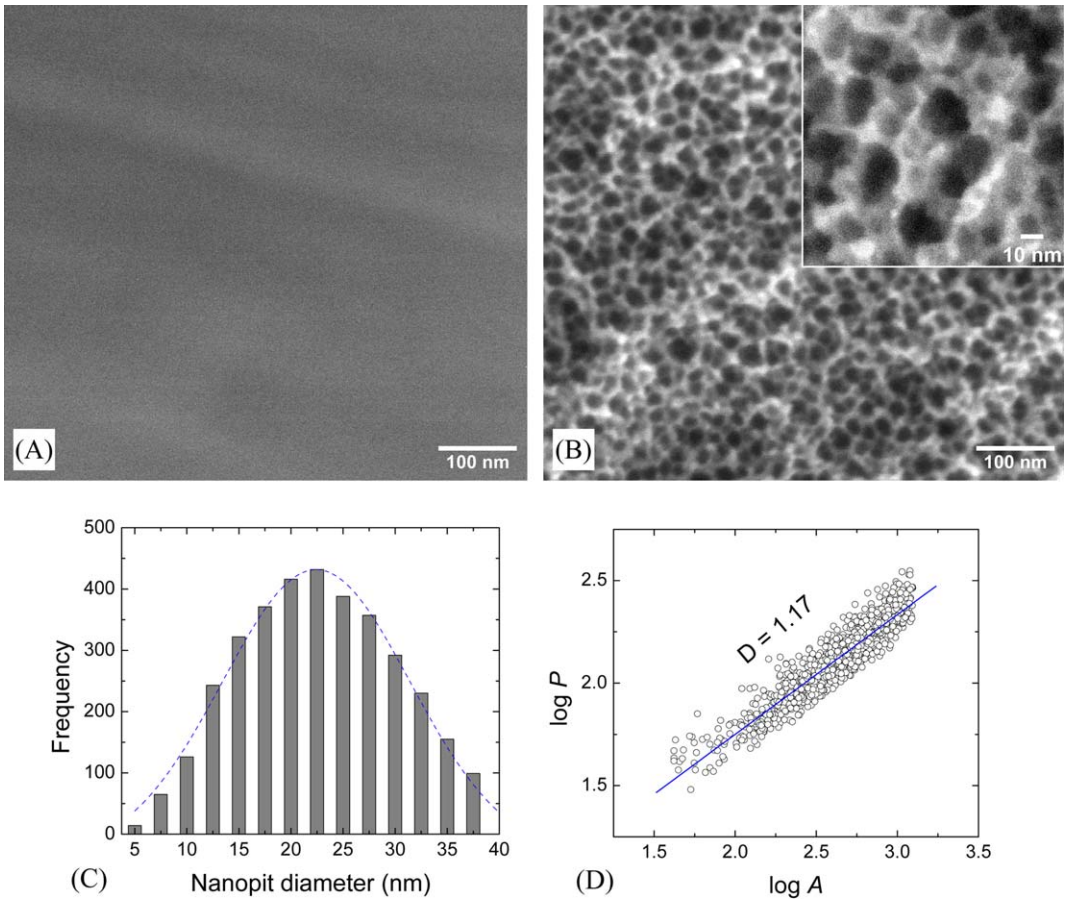

Fig. 5. SEM micrographs of control (A) and treated (B) cpTi surfaces. (C) Size distribution of nanopits in the image (B). (D) Fractal dimension of nanopits in the image (B).

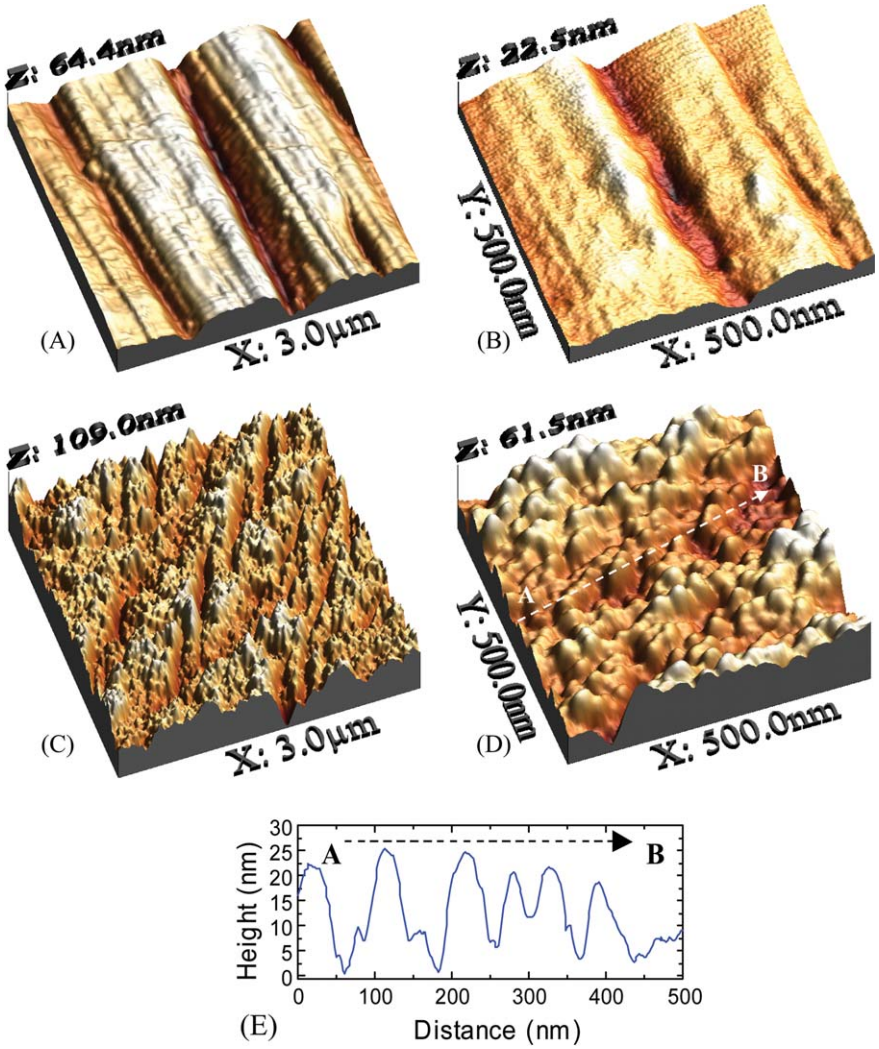

Fig. 6. AFM topographies of cpTi surfaces: (A) and (B) control, (C) and (D) treated. (E) Line scan height profile of A–B in the image (D).

observed on the untreated surface (Fig. 6A), whereas at both low and high magnification the treated surface showed texturing with no more traces of polishing (Fig. 6C and D). At high magnification ($500 \times 500\ nm^2$), the surface of untreated cpTi was found to be relatively smooth, with no grain–like structures (Fig. 6B). In contrast, Fig. 6D establishes that chemical treatment changes the surface topography completely, and the etched Ti surface consists of nano-sized peaks and pits. Quantitative changes in surface roughness (root mean square roughness, RMS) confirmed that a significant topographical alteration is produced by chemical treatment. Before etching, the sample showed a roughness value of ~5 nm, whereas it increased up to ~16 nm after etching. The line scan height profile shown in Fig. 6E reveals that the depth of the nanopits is in the 10–20 nm range.

4. Discussion

Chemical treatments such as acid etching and exposure to hydrogen peroxide and alkalis are known to produce textures on Ti surfaces [4,7,41]. In most cases, however, these treatments result in topographic features on the micron scale [42,43]. Our results show that chemical etching using H_2SO_4/H_2O_2 yields a nanotextured TiO_2 layer on the Ti surface. As summarized in Table 2, the physicochemical values of treated cpTi do not change significantly between the different samples, indicating that our chemical oxidation process has a high degree of reproducibility.

Table 2
Various extracted physicochemical values of the chemically oxidized Ti surfaces

Sample number	Ti:O ratio	Mean diameter of nanopits (nm)	Fractal dimensions of nanopits	Roughness (RMS, nm)	Estimated oxide layer thickness (nm)
# 1	1:2.08	22 ± 7	1.17 ± 0.01	16	40
# 2	1:2.02	20 ± 6	1.11 ± 0.01	17	32
# 3	1:2.03	21 ± 6	1.14 ± 0.01	20	41
# 4	1:2.05	21 ± 6	1.14 ± 0.01	14	32

Commercial Ti consists of polycrystalline grains with diameters of several microns. An amorphous native oxide layer, with a thickness of several nm, covers the Ti grains. This oxide layer is irregular in thickness and chemical composition [44,45]. Our chemical treatment was developed with the aim of removing the native oxide layer and recreating it under controlled conditions. To infer the surface oxide stoichiometry, we measured Ti:O ratios from XPS data before and after chemical treatment. Ti_{2p} spectra were used after removing the $Ti^{metallic}$ contribution (Fig. 1), and the O_{1s} spectra were used after removing the contributions of $O1s_{(OH)}$ and $O1s_{(H_2O)}$ (Fig. 2). An untreated control had a Ti:O ratio of 1:2.61, with the excess O presumably coming from carbon-containing contaminants. In contrast, the treated cpTi surface was found to have a Ti:O ratio of 1:2.08, confirming the formation of a highly pure TiO_2 layer on the Ti surface. As summarized in Table 2, all treated cpTi surfaces we analyzed have almost stoichiometric Ti:O ratios ranging between 1:2.02 and 1:2.08. This result indicates that our chemical etching with H_2SO_4/H_2O_2 is very effective, not only in removing the contaminated native oxide layer but also in generating essentially pure TiO_2 layers on Ti surfaces.

The thickness of the native oxide layer was estimated by XPS. However, the oxide layer on the treated cpTi was several times thicker and could not be measured by the same method, because the electron escape depth is only ~6 nm in the case of TiO_2 [28]. Weak $Ti^{metallic}$ peaks detected in the treated sample were probably due to the high porosity of the oxide layer.

An alternative approach to measuring the thickness of the oxide layer uses FTIR data. These data revealed that Ti–O bands increased significantly as a result of the chemical treatment. According to the Beer–Lambert Law, the path length of light (L) through a host material can be expressed as follows: [46]

$$L = A/\varepsilon c \tag{3}$$

where A is the maximum height of an absorption band or the area under the band; ε is the molar absorptivity; and c is the concentration. The sample thickness is thus proportional to the absorbance. Since the oxide layer of treated cpTi is composed of almost pure TiO_2 and that of untreated cpTi is composed of ~96 wt% TiO_2, both oxide layers are expected to have almost the same ε value. The ratio of the thicknesses of the oxide layers of the untreated and treated samples is therefore approximately equal to the ratio of absorbances. As the XPS and FTIR results revealed, the thickness of the native oxide layer was found to be ~5.0 nm, and the integral area ratio of Ti–O absorption bands in untreated and treated cpTi was in the 1:6.4–1:8.0 range, so the thickness of the TiO_2 layer on etched cpTi is estimated to be about 32–40 nm. However, the highly porous nature of the treated oxide layer suggests that its real thickness may exceed the estimated values. The thickness of oxide layers on Ti is known to play an important role in cell attachment [32], which is an essential parameter for osteogenic differentiation and tissue integration [47]. Recently, it has been reported that cell attachment as well as cell proliferation is enhanced as the thickness increases [48]. According to Kim et al., the binding strength of hydroxyapatite on Ti markedly improves when the oxide layer is thicker than the native oxide layer [49]. Furthermore, the resistance of Ti implants to corrosion is reported to increase with the thickness of the oxide layer [50]. It is therefore important to control the thickness of oxide layers to increase the bioactivity of Ti. Our chemical treatment provides an effective method for achieving this goal.

The mechanism by which mixtures of H_2SO_4/H_2O_2 create a nanotextured layer of TiO_2 is not fully understood. When Ti is exposed to H_2O_2 with or without acid, dissolution and oxidation of the metal occur [8,41], and the H_2O_2/acid/Ti reaction leads to the formation of a porous layer of TiO_2 on the Ti surface [35,41,51,52]. Usually this porous titania layer is known to be an amorphous phase that crystallizes as anatase when heated above ~300 °C [41,52]. Further heating above 600 °C leads to phase transition from anatase to rutile, which is the most stable form of titanium dioxide [41]. On the other hand, recent studies have revealed that titania can be crystallized at significantly lower temperatures. For example, Dhage et al. reported that refluxing titanium hydroxide gel induces the formation of anatase nanocrystallites at 100 °C [53]. Zuruzi et al. synthesized a porous TiO_2 layer on a Ti/Si substrate by means of aging in aqueous H_2O_2 solution at 80 °C, and they suggested that the as-formed titania layer consists of anatase nanocrystals in a largely amorphous titania matrix [52].

Since our XRD patterns of treated cpTi surfaces did not show any anatase or rutile peaks, the TiO_2 layer is thought to be amorphous. While the possibility that chemical oxidation by itself can lead to the formation of crystalline TiO_2 can not be excluded, the present results are consistent with the fact that the treatment was carried at ambient temperature which is not sufficient for crystallization of anatase. It will be interesting to see what happens when higher temperatures are used for oxidation. On the other hand, the Raman spectrum does not confirm unequivocally that the titania layer generated by chemical oxidation is completely amorphous. It should be noted that Raman spectroscopy is extremely sensitive to titania crystallites because of enhanced scattering associated with crystalline boundaries [54]. Two weak and broad Raman lines at ~290 cm^{-1} and ~610 cm^{-1} in Fig. 4B suggest that the largely amorphous titania layer may contain a few nanocrystallites. The low intensity and large FWMH of the Raman bands suggest that the crystallites, if present, are very small. Anatase has six Raman-active modes, among which four intense modes referred to as E_g (151 cm^{-1}), B_{1g} (409 cm^{-1}), A_{1g} or B_{1g} (515 cm^{-1}), and E_g (633 cm^{-1}) are usually detected for nanocrystalline anatase [55,56]. The Raman line at ~610 cm^{-1} in Fig. 4B seems to correspond to an E_g mode of anatase, whereas the attribution of the line at ~290 cm^{-1} remains unknown. Although the lower

frequency E_g band is known to be blue-shifted and broadened with decreasing crystallite size, our observed Raman line at $\sim$290 cm^{-1} is far from the normal value ($\sim$151 cm^{-1}). Further investigation using high-resolution transmission electron microscopy would be needed to fully elucidate the structure and crystalline phase of the TiO_2 layer.

5. Conclusions

This study shows that nanostructured surfaces can be obtained by simple chemical treatment. In order to better understand the effect that such surfaces have on cells and to develop methods to precisely control the properties of Ti-based biomaterials, we have characterized in detail their physicochemical properties. Further work is now in progress to control these underlying material properties, not only by varying the conditions of oxidation (etching time and temperature), but also by changing the oxidant and/or the acidity of the medium. Ongoing studies show that certain morphological properties such as average size and fractal dimensions of the nanopits can be controlled by varying the time of oxidation and concentration of reagents. Furthermore, results of cell culturing indicate a clear relationship between cell behavior and the morphological properties of the nanotextured Ti-based biomaterials [57]. We believe that it will be possible to control the properties of Ti surfaces, including the thickness of oxide layers, the size of nanopits, and the identity of the crystalline phases, by varying the precise conditions of the chemical treatment, and that this will lead to the creation of intelligent implant surfaces designed to influence cell activity rationally.

Acknowledgements

This work was supported by NSERC (Natural Sciences and Engineering Research Council of Canada) and CIHR (Canadian Institutes of Health Research). J.D.W. and F.R. acknowledge additional support from FQRNT and the Canada Research Chairs program.

References

[1] A. Nanci, M.D. Mckee, S. Zalzal, S. Sakkal, in: Z. Davidovitch, J. Mah (Eds.), Biological mechanisms of tooth eruption resorption and replacement by implants, Harvard Society for the Advancement of Orthodontics, Boston, 1998, p. 87.
[2] D.A. Puleo, A. Nanci, Biomaterials 20 (1999) 2311.
[3] T. Ishigaki, H. Haneda, N. Okada, S. Ito, Thin Solid Films. 390 (2001) 20.
[4] H.M. Kim, F. Miyaji, T. Kokubo, T. Nakamura, J. Biomed. Mater. Res. 32 (1996) 409.
[5] A. Nanci, J.D. Wuest, L. Peru, P. Brunet, V. Sharma, S. Zalzal, M.D. Mckee, J. Biomed. Mater. Res. 40 (1998) 324.
[6] M.E. Patsi, J.A. Hautaniemi, H.M. Rahiala, T.O. Peltola, I.M.O. Kangasniemi, J. Sol–Gel Sci. Tech. 11 (1998) 55.
[7] M. Takeuchi, Y. Abe, Y. Yoshida, Y. Nakayama, M. Okazaki, Y. Akagawa, Biomaterials 24 (2003) 1821.
[8] P. Tengvall, I. Lundstrom, L. Sjoqvist, H. Elwing, L.M. Bjursten, Biomaterials 10 (1989) 166.
[9] Y.S. Tian, C.Z. Chen, S.T. Li, Q.H. Huo, Appl. Surf. Sci. 242 (2005) 177.
[10] B.C. Yang, M. Uchida, H.M. Kim, X.D. Zhang, T. Kokubo, Biomaterials 25 (2004) 1003.
[11] J. Xu, J.Y. Rho, S.R. Mishra, Z. Fan, J. Biomed. Mater. Res. Part A 67A (2003) 719.
[12] S. Hengsberger, A. Kulik, P. Zysset, Eur. Cell Mater. 1 (2001) 12.
[13] T.J. Webster, E.L. Hellenmeyer, R.L. Price, Biomaterials 26 (2005) 953.
[14] T.J. Webster, L.S. Schadler, R.W. Siegel, R. Bizios, Tissue Eng. 7 (2001) 291.
[15] T.J. Webster, J.U. Ejiofor, Biomaterials 25 (2004) 4731.
[16] M.J. Dalby, M.O. Riehle, H. Johnstone, S. Affrossman, A.S.G. Curtis, Biomaterials 23 (2002) 2945.
[17] M.J. Dalby, S.J. Yarwood, M.O. Riehle, H.J.H. Johnstone, S. Affrossman, A.S.G. Curtsi, Exp. Cell Res. 276 (2002) 1.
[18] K.L. Elias, R.L. Price, T.J. Webster, Biomaterials 23 (2002) 3279.
[19] M.J. Dalby, D. McCloy, M. Robertson, C.D.W. Wilkinson, R.O.C. Oreffo, Biomaterials 27 (2006) 1306.
[20] T.K. Monsees, K. Barth, S. Tippelt, K. Heidel, A. Gorbunov, W. Pompe, R.H.W. Funk, Cells Tissues Organs 180 (2005) 81.
[21] A.S. Andersson, F. Backhed, A. von Euler, A. Richter-Dahlfors, D. Sutherland, B. Kasemo, Biomaterials 24 (2003) 3427.
[22] G. Giavaresi et al., Biomaterials 25 (2004) 5583.
[23] F. Rosei, J. Phys. : Conden. Mater. 16 (2004) S1373–S1436.
[24] P.T. De Oliveira, A. Nanci, Biomaterials 25 (2004) 403.
[25] D. Briggs, M.P. Seah, Practical Surface Analysis, Wiley, Chichester, 1990.
[26] K.M. Davis, M. Tomozawa, J. Non-Cryst. Solids 201 (1996) 177.
[27] N.C. Kenkel, D.J. Walker, Coenoses 11 (1996) 77.
[28] C. Sittig, M. Textor, N.D. Spencer, M. Wieland, P.H. Vallotton, J. Mater. Sci. Mater. Med. 10 (1999) 35.
[29] D.S. Sutherland, P.D. Forshaw, G.C. Allen, I.T. Brown, K.R. Williams, Biomaterials 14 (1993) 893.
[30] J. Pouilleau, D. Devilliers, F. Garrido, S. DurandVidal, Mater. Sci. Eng. B 47 (1997) 235.
[31] P. Martin, M. Dufour, A. Ermolieff, S. Marthon, F. Pierre, M. Dupuy, J. Appl. Phys. 72 (1992) 2907.
[32] X.Y. Liu, P.K. Chu, C.X. Ding, Mater. Sci. Eng. R 47 (2004) 49.
[33] B. Gallas, A. Brunet-Bruneau, S. Fisson, G. Vuye, J. Rivory, J. Appl. Phys. 92 (2002) 1922.
[34] W.J. Zhang, Y. Li, S.L. Zhu, F.H. Wang, Surf. Coat. Technol. 182 (2004) 192.
[35] J. Pan, H. Liao, C. Leygraf, D. Thierry, J. Li, J. Biomed. Mater. Res. 40 (1998) 244.
[36] M. Tanahashi, T. Yao, T. Kokubo, M. Minoda, T. Miyamoto, T. Nakamura, T. Yamamuro, J. Biomed. Mater. Res. 29 (1995) 349.
[37] S. Watson, D. Beydoun, J. Scott, R. Amal, J. Nanoparticle Res. 6 (2004) 193.
[38] M. Nakamura, T. Aoki, Y. Hatanaka, D. Korzec, J. Engemann, J. Mater. Res. 16 (2001) 621.
[39] R. Urlaub, U. Posset, R. Thull, J. Non-Cryst. Solids 265 (2000) 276.
[40] L. Sirghi, T. Aoki, Y. Hatanaka, Surf. Rev. Lett. 10 (2003) 345.
[41] X.X. Wang, S. Hayakawa, K. Tsuru, A. Osaka, Biomaterials 23 (2002) 1353.
[42] D.H. Li, S.J. Ferguson, T. Beutler, D.L. Cochran, C. Sittig, H.P. Hirt, D. Buser, J. Biomed. Mater. Res. 60 (2002) 325.
[43] S. Szmukler-Moncler, T. Testori, J.P. Bernard, J. Biomed. Mater. Res. Part B 69B (2004) 46.
[44] N.L.H. Degatica, G.L. Jones, J.A. Gardella, Appl. Surf. Sci. 68 (1993) 107.
[45] B. Walivaara, B.O. Aronsson, M. Rodahl, J. Lausmaa, P. Tengvall, Biomaterials 15 (1994) 827.
[46] B. Stuart, Modern Infrared Spectroscopy, John Wiley & Sons Ltd., Dartford, 1996.
[47] C. Modin et al., Biomaterials 27 (2006) 1346.
[48] X.L. Zhu, J. Chen, L. Scheideler, R. Reichl, J. Geis-Gerstorfer, Biomaterials 25 (2004) 4087.

[49] L.H. Li, Y.M. Kong, H.W. Kim, Y.W. Kim, H.E. Kim, S.J. Heo, J.Y. Koak, Biomaterials 25 (2004) 2867.
[50] M. Cabrini, A. Cigada, G. Rondelli, B. Vicentini, Biomaterials 18 (1997) 783.
[51] J. Pan, D. Thierry, C. Leygraf, J. Biomed. Mater. Res. 30 (1996) 393.
[52] A.S. Zuruzi, N.C. MacDonald, Adv. Funct. Mater. 15 (2005) 396.
[53] S.R. Dhage, V.D. Choube, V. Samuel, V. Ravi, Mater. Lett. 58 (2004) 2310.
[54] X.T. Gao, I.E. Wachs, Catal. Today 51 (1999) 233.
[55] H.C. Choi, Y.M. Jung, S.B. Kim, Vibrat. Spectrosc. 37 (2005) 33.
[56] W.F. Zhang, Y.L. He, M.S. Zhang, Z. Yin, Q. Chen, J. Phys. D – Appl. Phys. 33 (2000) 912.
[57] L. Richert, J.H. Yi, J.D. Wuest, F. Rosei, A. Nanci, Modulation of fibroblast activity by nanotextured titanium alloy. in: 52nd Annual Meeting of the Orthopaedic Research Society. Chicago, IL, May 19–22, 2006.